Additive Manufacturing 29 (2019) 100770

Contents lists available at ScienceDirect

Additive Manufacturing

journal homepage: www.elsevier.com/locate/addma

Multi-scale computational modeling of residual stress in selective laser melting with uncertainty quantification

Daniel Moser[a,*], Michael Cullinan[b], Jayathi Murthy[c]

[a] Sandia National Laboratories, P.O. Box 5800, Albuquerque, NM 87185, United States
[b] The University of Texas at Austin Mechanical Engineering, 204 E. Dean Keeton Street, Stop C2200, ETC II 5.160, Austin, TX 78712, United States
[c] UCLA Mechanical and Aerospace Engineering Department, BOX 951597, 48-121 E4, Los Angeles, CA 90095-1597, United States

ARTICLE INFO

Keywords:
Uncertainty quantification
Selective laser melting
Computational modeling

ABSTRACT

Selective laser melting (SLM) is a powder-based additive manufacturing technique which creates parts by fusing together successive layers of powder with a laser. The quality of produced parts is highly dependent on the proper selection of processing parameters, requiring significant testing and experimentation to determine parameters for a given machine and material. Computational modeling could potentially be used to shorten this process by identifying parameters through simulation. However, simulating complete SLM builds is challenging due to the difference in scale between the size of the particles and laser used in the build and the size of the part produced. Often, continuum models are employed which approximate the powder as a continuous medium to avoid the need to model powder particles individually. While computationally expedient, continuum models require as inputs effective material properties for the powder which are often difficult to obtain experimentally. Building on previous works which have developed methods for estimating these effective properties along with their uncertainties through the use of detailed models, this work presents a part scale continuum model capable of predicting residual thermal stresses in an SLM build with uncertainty estimates. Model predictions are compared to experimental measurements from the literature.

1. Introduction

Free-form fabrication techniques such as selective laser melting (SLM) have seen increasing use across industries as they enable the production of parts directly from computer-aided design (CAD) models without specific tooling. While a number of such techniques have been developed, SLM is a powder-based technology in which a laser is used to melt selected regions of a deposited powder bed based on a geometric model. Re-solidification of the melt forms the part. Powder is added and melted layer by layer until a full part is built [1].

SLM faces a number of challenges as improper selection of processing parameters, such as laser power, speed, or scan path, can lead to geometric defects, pore formation, and warping or part weakness due to thermal stress. Currently, parameters for a given part, material, and machine are determined through a dial-in process in which test parts are constructed with different machine settings and their properties measured until settings are found that produce acceptable results [1]. Computational modeling has the potential to reduce the costs and time required to dial in new geometries and materials by predicting the performance of parts produced using a specific set of parameters in advance of a build. Models could also be used to inform automatic process control schemes [2].

There are broadly two approaches to modeling the SLM process, continuum models and particle-scale models. Continuum models approximate a powder bed as a continuous medium, neglecting individual particles. Numerous continuum models of laser-powder additive manufacturing processes have already been developed. For example, Sun et al. [3] used a 3D finite element model implemented in ANSYS to predict the temperature profile and melting of an aluminum alloy for a complex geometry. Zeng et al. [4] used adaptive meshing techniques to resolve the thermal gradients near the laser. Hodge et al. [5] introduced a thermo-mechanical model to calculate part residual stresses. In all of these works, however, simple approximations were used to determine the effective powder properties required by the continuum model and no quantification of uncertainties was performed.

Particle-scale models, on the other hand, resolve individual particles in the domain and often encompass detailed physics. While using a particle-scale model to simulate a full-scale part build would be too computationally expensive, particle-scale models of small portions of SLM powder beds have had success in qualitatively explaining some

* Corresponding author.
E-mail address: dmoser@sandia.gov (D. Moser).

https://doi.org/10.1016/j.addma.2019.06.021
Received 11 December 2018; Received in revised form 4 April 2019; Accepted 24 June 2019
Available online 08 July 2019

phenomena occurring at the particle level (e.g. Khairallah et al. [6] who used particle-scale models to investigate the physics behind spatter and pore formation). Others have used particle-scale models to calculate effective properties needed in continuum models [7–9]. This work presents a framework in which effective properties determined from particle-scale simulations are used to make residual stress predictions with a continuum model. Uncertainties calculated for effective parameters are propagated through the continuum model using Gaussian process surrogate models [10], allowing the effects of uncertainties at the particle-scale to be assessed at the continuum level and quantitative comparison to experimental data to be made.

2. Modeling approach

2.1. Mathematical model

The temperature in the SLM powder bed is calculated using the energy equation, cast in the enthalpy formulation to better account for latent heats of phase change [11].

$$\frac{\partial H}{\partial t} = \nabla\cdot(k_{\text{eff}}\nabla T) + f(x, y, z, t) \tag{1}$$

$H(x, y, z, t)$ is the enthalpy of the material, $T(x, y, z, t)$ the temperature, $f(x, y, z, t)$ the heat source due to the laser, and k_{eff} the thermal conductivity of the powder. k_{eff} is often not known for a powdered material and will be informed by a particle-scale model. The top boundary of the domain has convective-radiative boundary conditions applied. The bottom boundary is fixed temperature at 300 K, and the remaining boundaries are insulated. This is shown in Fig. 1.

The enthalpy formulation requires a relation between enthalpy and temperature, which is given by [11]

$$H = (1 - g(T))\int_{T_{\text{ref}}}^{T} \rho c_s \mathrm{dT} + g(T)\int_{T_{\text{ref}}}^{T} \rho c_l \mathrm{dT} + g(T)\rho L \tag{2}$$

$g(T)$ is the melt fraction, c_s and c_l are the solid and liquid specific heats, and L is the latent heat. Powder heat capacities (ρc_s) are calculated using volume averaging, as given by Eq. (8). In order to determine a relation between melt fraction and temperature, the lever rule is used, $g(T) = \frac{T - T_s}{T_l - T_s}$, for T between T_s, the solidus temperature, and T_l, the liquidus temperature. $g(T)$ is zero below T_s and one above T_l.

A Gaussian laser heat source is used for $f(x, y, z, t)$ [12].

$$f = \alpha I_0 \beta \exp\left(-2\frac{(x - x_l)^2 + (y - y_l)^2}{\omega^2} - \beta z\right) \tag{3}$$

I_0 is the laser intensity, α powder bed optical absorptivity, x_l and y_l give the laser position, ω is the standard deviation of the Gaussian, and β is the optical extinction coefficient. Similar to k_{eff}, α and β are unknown for most powder materials and results from particle-scales models will be used to determine them.

A continuum mechanical model coupled to the thermal model is used to make residual stress predictions in built parts. The mechanical model uses Hooke's law for elastic, isotropic, materials to relate the incremental strain, the change in strain over a time increment, $\Delta\boldsymbol{\epsilon}$, to the incremental stress as given in Eq. (4).

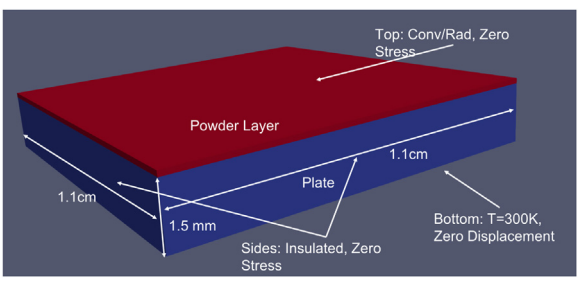

Fig. 1. Simulation domain showing boundary conditions.

$$\Delta\boldsymbol{\sigma} = 2\mu(\Delta\boldsymbol{\epsilon} - \Delta\boldsymbol{\epsilon}^p - \Delta\boldsymbol{\epsilon}^t) + \lambda\boldsymbol{I}\mathrm{tr}(\Delta\boldsymbol{\epsilon} - \Delta\boldsymbol{\epsilon}^p - \Delta\boldsymbol{\epsilon}^t) \tag{4}$$

λ and μ are Lamé's parameters, $\Delta\boldsymbol{\epsilon}^e$ and $\Delta\boldsymbol{\epsilon}^p$ are the elastic and plastic strain increments, and $\Delta\boldsymbol{\epsilon}^t$ is the increment of thermal strain, which provides the coupling to the energy equation and is calculated from the temperature using Eq. (5) [13].

$$\Delta\boldsymbol{\epsilon}^t = \int_{T_1}^{T_2} a(T)\mathrm{dT} \tag{5}$$

T_1 and T_2 are the temperatures at the start and end of a time increment and a is the coefficient of thermal expansion.

The plastic strain increment, $\Delta\boldsymbol{\epsilon}^p$, is calculated using a J2 plasticity model by enforcing the inequality that the von Mises equivalent stress not exceed the yield strength.

$$\sqrt{\frac{3}{2}\boldsymbol{s}:\boldsymbol{s}} \leq \sigma_y \tag{6}$$

$\boldsymbol{s}$ is the deviatoric of the total stress, $\boldsymbol{\sigma} + \Delta\boldsymbol{\sigma}$, and $\sigma_y(T, \boldsymbol{\epsilon}^p)$ is the yield strength of the material. A temperature-dependent linear strain-hardening relation is used such that $\sigma_y = \sigma_y^0(T) + \kappa|\boldsymbol{\epsilon}^p|$.

The stress increment can then be related to the displacement increment through Newton's law.

$$0 = \nabla\cdot\Delta\boldsymbol{\sigma} \tag{7}$$

Zero stress boundary conditions are imposed on all domain boundaries except for the bottom boundary, where a zero displacement condition is used, simulating attachment to a large baseplate. This is shown in Fig. 1.

2.2. Implementation details

A finite volume discretization scheme using the OpenFOAM finite volume library is used for all the governing equations [14,15]. The domain is divided into hexahedral cells and the equations integrated over them to form a linear system that is solved iteratively. The energy equation is solved using a diagonal incomplete LU (DILU) preconditioned, stabilized conjugate gradient solver. The three components of the displacement in the mechanical equations are solved coupled using a DILU preconditioned, stabilized bi-conjugate gradient solver. The spatial discretization is first order and a backwards Euler time integration scheme is used. The equations are solved segregated, with the temperature field computed first and transferred to the mechanical solver since the mechanical governing equations depend on the thermal solution, but not visa-versa.

The model is multi-phase consisting of powder, solidified metal, and a background gas (usually air or nitrogen). Simulations are initialized with a single layer of powder on top of a solid metal base. For multi-layer simulations, after the laser scans the first layer, a new domain is initialized with an additional layer of powder and the solution from the last time step of the previous layer simulation is copied over to act as the new initial condition. Material properties are calculated based on location in the domain. Cells that fall in the powder layer are assigned powder properties and cells that lie in the plate are assigned solid metal properties. Powder cells are initially considered to be a separate phase from metal and air. However, once melting occurs, powder volume fractions are converted to solid and air volume fractions, depending on the prescribed powder porosity. The melt fraction, $g(T)$, for the powder is tracked in each cell to determine when volume fractions should be converted. The initialization, melting, and layer addition processes are shown in Fig. 2.

Volume averaging is used to calculate material properties of cells that contain mixtures of materials. This is given in Eq. (8).

$$\zeta_{\text{total}} = \gamma_{\text{powder}}\zeta_{\text{powder}} + \gamma_{\text{solid}}\zeta_{\text{solid}} + (1 - \gamma_{\text{powder}} - \gamma_{\text{solid}})\zeta_{\text{air}} \tag{8}$$

γ is the volume fraction of a material and ζ is a given material property.

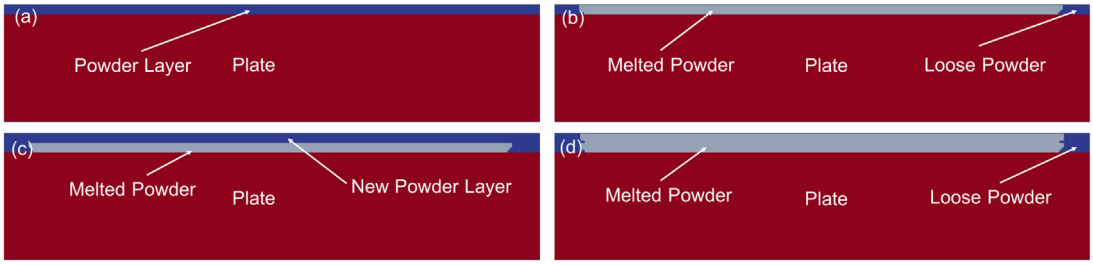

Fig. 2. (a) Initial domain with 1 layer of powder on a solid plate. (b) Domain after completion of 1 layer scan. Melted and loose powder on solid plate. (c) Domain after 1 layer addition. Loose powder on top of previously melted powder. (d) Domain after completion of 2 layer scans. Two layers of melted powder on solid plate.

Table 1
316 stainless steel thermal properties.

Property	Value
Density	7.43 g/cm^3
Thermal conductivity	20.0 W/m K
Specific heat	320.3 + 0.379T J/kg K (T in K)
Emissivity	0.3–0.6 (uniform random)
Latent heat	270 kJ/kg
Solidus temperature	1648 K
Liquidus temperature	1673 K

The energy equation is nonlinear due to the dependence of the enthalpy term on temperature, which is solved following the method of Swaminathan and Voller [11]. In each iteration, the enthalpy term is expressed using a truncated Taylor series expansion.

$$H^{i+1} = H^i + \frac{\mathrm{dH}^i}{\mathrm{dT}}\left[T^{i+1} - T^i\right] \tag{9}$$

where i and $i+1$ refer to the previous iteration and current iteration, respectively. This allows the enthalpy terms to be accounted for partially implicitly to improve stability and convergence. The temperature solution is iterated until the temperature and enthalpy fields are consistent to within a prescribed tolerance.

The plastic nonlinearity in the mechanical model is solved using the elastic predictor-plastic corrector method. In each cell, a trial stress is calculated for a fully elastic response and the von Mises equivalent stress computed. In cells where the inequality of Eq. (6) is violated, a plastic strain increment is calculated and imposed that returns the stress to the yield surface [13]. The stress increment is then updated for the next iteration and the process repeated until the change in the displacement field is below a prescribed tolerance.

The temperature and displacement fields are solved for over the entire domain at each time step. This requires that, for the mechanical model, Lamé's parameters, μ and λ, must be specified for the entire domain, including the powder and air cells. However, these quantities are only well defined for a solid. To address this, Lamé's parameters are set to be 3 orders of magnitude smaller than the solid material values in the air and powder regions. It is determined that making them smaller has little impact on the solution and slows convergence. Air and powder cells thus provide very little resistance to deformation. They are also set to have arbitrarily large yield strengths and zero coefficients of thermal expansion, so they do not undergo thermal expansion or plastic deformation.

3. Results

3.1. Problem description

The model results are compared against the experimental data of Yadroitsava et al. [16], who measured experimentally the residual stress in stainless steel 316 powder melted onto a stainless steel substrate using SLM for both a single layer and 5 layers. The layer thickness used is 40 μm and the size of the area being melted is 1 cm × 1 cm. Specimens were constructed using a simple back-and-forth hatching scan pattern with no rotation of the hatch pattern between layers. Residual stresses were measured in directions parallel and perpendicular to the laser scan direction in the plane of the powder bed. Measurements were made with a ProtoXRD X-ray diffractometer using the $sin^2\phi$ method. For single layers, measurements were made at the center of the part, both at the bottom of the layer, near the baseplate, and at the top, near the free surface. For 5 layer parts, measurements were additionally made approximately 100 μm from the free surface [16].

In order to compare to Yadroitsava's data, simulations are conducted for 316 stainless steel powder. Thermal properties are given by Khairallah et al. [17,6] for temperatures up to the vaporization temperature and summarized in Table 1. Mechanical properties are given by Hodge et al. [5]. Per Hodge et al, mechanical property data for 316 stainless steel are difficult to find at temperatures near the melt point. Thus, Hodge et al. provides extrapolated values for temperatures above the measurement range found in the literature (approximately 1300 K) up to the melt point [5]. Above the melt point, the material is considered liquid and Lamé's parameters are set arbitrarily low as is done for powder and air cells. Properties such as Young's modulus and yield strength are temperature dependent, so polynomial curve fits are applied to Hodge's mechanical property values to create functions that can be used by the simulation.

Significant uncertainty exists in the mechanical properties used in the simulation. Not only are high-temperature data not available, but properties of additively manufactured materials are known to differ from those of wrought materials. Mower and Long [18] measured the yield strength, Young's modulus, ultimate strength, and failure strain of both wrought 316 stainless steel and specimens manufactured using laser powder bed fusion at room temperature. From these values, uncertainties in yield strength, Young's Modulus, and strain hardening coefficient are estimated by making the constant coefficient in the polynomial functions derived from Hodge et al. [5] a Gaussian random variable whose mean is selected such that the expected value of each property at 300 K is the average of the value from Hodge et al. [5] and that measured by Mower and Long [18] for additively manufactured 316 stainless steel. Standard deviations are selected to be half of the difference between the Hodge et al. and Mower and Long values. As no data were found in the literature for coefficients of thermal expansion of additively manufactured materials, uncertainty in this quantity is not considered. Mechanical properties used in the simulation are summarized in Table 2. Laser parameters used in the simulation are chosen to match those used by Yadroitsava and are summarized in Table 3.

3.2. Computational details

The powder layer is meshed using a uniform mesh size of 10 μm and a constant time step size of 0.001 s is used. This is selected as further mesh and temporal refinement results in variations of less than 5% for the maximum value of both the temperature and stress solutions. The initial computational domain consists of approximately 5 million cells

Table 2
316 stainless steel mechanical properties.

Property	Value
Young's modulus	2.204e11 − 9.3795e7T ± 1.0e10 Pa (T in K) (Gaussian random)
Coefficient of thermal expansion	1.2989e−5 + 8.4443e−9T − 2.8339e−12T^2 1/K (T in K)
Yield strength	5.3394e8 − 6.004e5T + 3.9859e2T^2 − 0.1143T^3 ± 1.13e8 Pa (T in K) (Gaussian random)
Strain hardening coefficient	7.4e8 ± 5.0e7 Pa (Gaussian random)
Poisson's ratio	0.3

Table 3
Laser properties for stainless steel stress calculations [16].

Property	Case 1
Power	50 W
Speed	10 cm/s
Beam diameter (FWHM)	70 μm
Hatch spacing (distance between successive laser scan lines)	70 μm

and approximately 15,000 time steps are needed to complete the scan of a layer.

3.3. Effective powder properties

While most effective powder properties are calculated by volume averaging the properties of steel and air, the extinction coefficient, thermal conductivity, and absorption coefficient are not accurately approximated using this method [19]. These parameters are instead calculated using particle-scale models. Moser et al. [7] developed a method for modeling interactions between a laser and powder particles. The method uses the discrete element method (DEM) to represent powder particles and ray-tracing to simulate a laser. Powder beds are generated and laser rays propagated through them by calculating ray-sphere intersections. On every ray-sphere interaction, a portion of the ray energy is absorbed and a portion reflected to propagate further in the domain. By tracking the deposition of energy in the domain, effective absorptivites and extinction coefficients for powders can be obtained. Based on this analysis, a correlation was derived between effective powder absorptivity and solid metal absorptivity and is given in Eq. (10).

$$\alpha_{\text{eff}} = 0.053 + 1.37\alpha - 1.04\alpha^2 + 0.399\alpha^3 \pm 0.02 \tag{10}$$

Similarly, a correlation between the effective powder extinction coefficient, solid metal absorptivity, and the average radius of the powder particles was derived and is given in Eq. (11). Although this relation was developed for monodisperse particle beds, Moser et al. [7] found the additional uncertainty due to polydispersity to be small for size variation less than the average particle radius.

$$\beta R = 0.325 + 1.03\alpha - 1.22\alpha^2 + 0.587\alpha^3 \pm 0.02 \tag{11}$$

However, the absorptivity of 316 stainless steel is itself an uncertain quantity which varies based on the surface properties of the metal. As given in Table 1, this quantity is approximated as a uniform random variable between 0.3 and 0.6. In order to calculate the probability distributions of the effective powder absorptivity and extinction coefficient, samples are randomly drawn from the stainless steel absorptivity distribution and each sample is used to calculate a powder absorptivity and extinction coefficient using Eqs. (10) and (11). The uncertainties of 0.02 in each of the equations are approximated as Gaussian random variables with means of zero and standard deviations of 0.02. After an effective absorptivity or extinction coefficient is calculated for a sample, a sample is drawn from the Gaussian distribution and added to the result. This process is repeated for subsequent samples to create a histogram of effective absorptivity and extinction coefficient values. These histograms are then normalized by the total number of samples drawn to create an approximation of the probability density functions of these quantities, as shown in Fig. 3.

Moser et al. [8] also developed a method for calculating effective thermal conductivities of powders using the DEM to represent powder particles. Powder beds are generated and thermal gradients imposed across them. Relations for heat transfer between particles due to particle-particle contact, conduction through the background gas, and radiation are used to calculate the resulting heat flux and thus the effective thermal conductivity. Based on this analysis, a correlation was developed between the metal conductivity (k_s), gas conductivity (k_g), particle diameter (D_p), temperature (T), and powder conductivity (k_{eff}) and is given in Eq. (12).

$$\frac{k_{\text{eff}}}{k_s} = -2.44\theta^2 + 15.2\theta\kappa + 3.57\theta - 25.2\kappa^2 + 11.7\kappa + 0.001 \pm 11\% \tag{12}$$

where θ and κ are non-dimensional quantities given by: $\theta = \frac{\sigma T^3 D_p}{k_s}$ and $\kappa = \frac{k_g}{k_s}$. This relation was also developed for monodisperse particle beds, but the additional uncertainty due to polydispersity was also found to be small for size variation less than the average particle radius.

The variation of thermal conductivity with temperature between room temperature and melt is found to be smaller than the uncertainty in the correlation, thus the additional uncertainty of not considering temperature dependent powder conductivity is minimal. Therefore, the continuum thermo-mechanical model does not consider temperature-

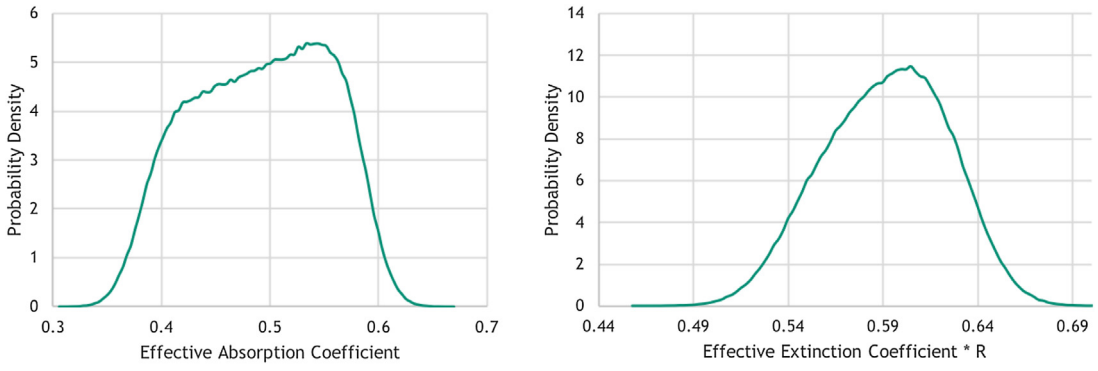

Fig. 3. Probability density functions for powder absorptivity and extinction coefficient.

dependent thermal conductivities in order to allow faster convergence of the thermal model. The powder effective conductivity is computed at a temperature of 974 K, halfway between room temperature (300 K) and the solidus temperature of 316 stainless steel. Powder conductivity is then taken to be a Gaussian random variable with mean 0.32 and standard deviation 0.04 W/m K.

3.4. Uncertainty quantification

Once the continuum model input probability distributions are known, they must be propagated through the model in order to estimate uncertainties of the model outputs. The goal is to compute statistical quantities, such as mean and standard deviation, for each model prediction. This can be done by drawing samples from the input distributions, evaluating the model with the selected inputs, and computing statistics from the model outputs. Due to the large computational cost of the model, however, this approach is not tractable as large numbers of evaluations are needed for the statistics to converge. Instead, a surrogate model is constructed. Due to the high dimensionality of random input parameter space, a Gaussian process surrogate model from the Dakota open source toolkit is used [20].

A Gaussian process surrogate approximates the response of a model, Φ, as a function of the random input variables, $\boldsymbol{\zeta}$, using a combination of trend functions and an error model [20].

$$\Phi \approx \boldsymbol{g}(\boldsymbol{\zeta})^T\boldsymbol{\beta} + \boldsymbol{r}(\boldsymbol{\zeta})^T\boldsymbol{R}^{-1}(\boldsymbol{f} - \boldsymbol{G}\boldsymbol{\beta}) \tag{13}$$

$\boldsymbol{g}(\boldsymbol{\zeta})$ is a set of trend functions evaluated at the current values of the input variables and $\boldsymbol{\beta}$ are the coefficients of the trend functions. Together, these define a response surface which provides an approximation of the true model response over large-scale variations in the input parameters. For this application, a reduced quadratic trend function basis is used, meaning that the function contains terms that are linear and quadratic in each of the input parameters, but all interaction terms are omitted. Thus, constructing the trend function requires $2n + 1$ model evaluations, where n is the number of random input parameters. However, in general more than the minimum number of model evaluations are performed, thus requiring $\boldsymbol{\beta}$ to be determined using a least squares fit [20].

When a least squares fit is used, the surrogate model will not exactly interpolate the model evaluations used to construct it. Thus, an error model is introduced which adjusts the trend function so that the surrogate exactly interpolates the evaluations. $\boldsymbol{r}(\boldsymbol{\zeta})^T$ in Eq. (13) is a correlation vector between $\boldsymbol{\zeta}$, the current input parameters, and the parameter values used in the model evaluations. $\boldsymbol{R}$ is a correlation matrix of all of the model evaluation points, and $(\boldsymbol{f} - \boldsymbol{G}\boldsymbol{\beta})$ is the difference between the approximations return by the trend function and the actual model evaluations at each of the evaluation points. Dakota uses a Gaussian correlation function to model the correlation [10].

$$r(\boldsymbol{X_i}, \boldsymbol{X_j}) = \exp\left(-\sum_{k=1}^{n} \theta_k [\boldsymbol{X_{i,k}} - \boldsymbol{X_{j,k}}]^2\right) \tag{14}$$

where n is the number of random input parameters, $\boldsymbol{X_{i,k}}$ is a matrix made up of the model evaluation points, and θ_k are n parameters of the surrogate model calculated using a maximum likelihood estimation procedure.

Considering the parameters needed by the trend function and the error model, $3n + 1$ model evaluations are required to fully inform the surrogate model. For this work with six uncertain variables, a minimum of 19 evaluations are needed. In order to ensure surrogate model accuracy, 30 evaluations are performed to build the surrogate model and an addition 4 to assess its accuracy. Model evaluation points are selected using the Latin Hypercube sampling method in which the range of each uncertain variable is divided into equal probability intervals and a sample drawn randomly from within each one [10]. A surrogate constructed using 30 evaluations is found to differ on average 10% from the model across the quantities of interest and the 4 test evaluations. This is deemed sufficient accuracy as the surrogate is being used only to estimate uncertainties.

After the surrogate model is constructed, moment statistics are calculated by Monte Carlo sampling. Since the surrogate is inexpensive to evaluate, thousands of samples can be performed in order to calculate the mean and standard deviation of each quantity of interest, providing an estimate of the range of the model predictions possible given the specified input parameter uncertainties.

The contribution of each random input parameter to the overall uncertainty in the quantities of interest is also calculated using variance based decomposition (VBD). VBD defines the main effect, S, of an input parameter, ζ, on a model response Φ as given in Eq. (15), and is the fraction of the uncertainty in output Φ due to ζ alone. VBD defines the total effect, T, of ζ on Φ as given in Eq. (16), and is the fraction of the uncertainty in output Φ due to interactions between ζ and other inputs [20].

$$S_i = \frac{\mathrm{Var}_{\zeta_i}[E(\Phi|\zeta_i)]}{\mathrm{Var}(\Phi)} \tag{15}$$

$$T_i = \frac{E(\mathrm{Var}(\Phi|\zeta_1,...,\zeta_{i-1},\zeta_{i+1},...,\zeta_n))}{\mathrm{Var}(\Phi)} \tag{16}$$

The variances and expected values required by VBD are also calculated using Monte Carlo sampling.

The response quantities of interest for this work are the residual stresses parallel and perpendicular to the path of the laser both near the powder-baseplate interface and near the top of the domain. For the five layer case, additional quantities of interest are the stresses approximately 100 μm from the top of the domain.

3.5. Stress predictions

The action of the laser in the simulation creates overlapping melt tracks of melted powder. Fig. 4 shows the laser spot as the laser performs a line scan along the powder layer.

Repeated, overlapping laser line scans result in a recurring pattern of residual stress distributions as shown in Fig. 5 from the top and Fig. 6 along a cross section.

Since it is not known exactly where the measurements of Yadroitsava et al. were taken relative to the laser scans, calculated residual stresses are averaged across a laser track to calculate mean residual stress values as well as standard deviations of those means. These standard deviations due to position are added in quadrature with the standard deviations due to the uncertain model input parameters calculated using the surrogate model method discussed previously to determine an overall standard deviation on the residual stress predictions. The predicted stress profiles in the consolidated powder layer from baseplate to free surface are shown in Fig. 7 for the single layer case.

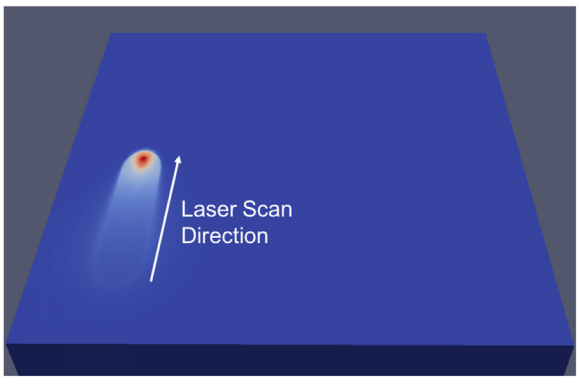

Fig. 4. Laser spot on powder bed surface.

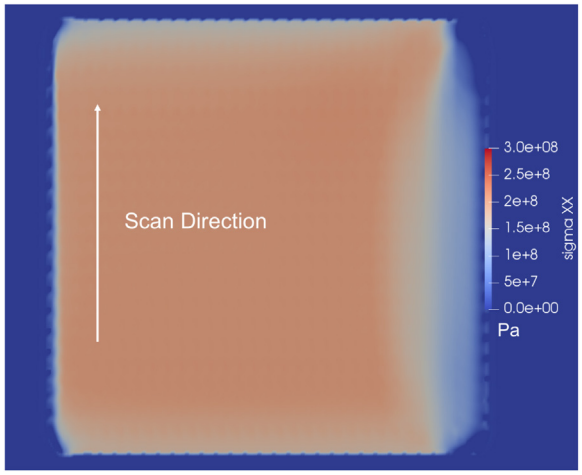

Fig. 5. Residual stress top view.

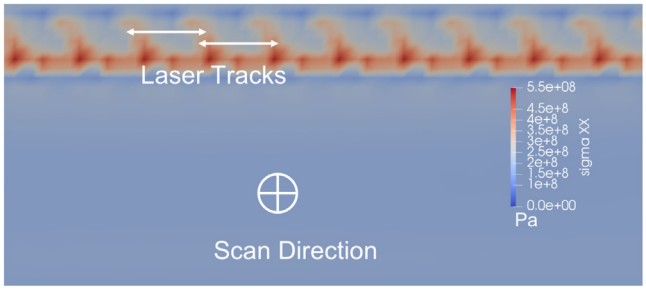

Fig. 6. Residual stress cross section showing results of overlapping laser scans. Arrows indicate the width of a scan line.

The shaded region indicates one standard deviation. The range of Yadroitsava's measurements near the plate and near the free surface are shown as horizontal lines.

As can be seen, the model predictions fall within one standard deviation of the experimental data near the baseplate. Near the free surface, predicted residual stresses fall off quickly in both cases over the last 10 μm of height as the zero stress boundary allows the material to deform freely to relieve stress. It is unknown the exact height at which the measurement was taken, but the experimental and model results do overlap to within a standard deviation for the entire range 30–40 μm from the substrate for both the parallel and perpendicular cases. Thus, the model results do agree with the available experimental data, given the estimated uncertainties. It should be noted, however, that the combined uncertainties due to model inputs and the location of the measurement taken relative to the laser scan pattern are large, limiting the precision of the model prediction.

The results from the 5 layer case are shown in Fig. 8. Again, the shaded regions represent one standard deviation and Yadroitsava's measurements are shown as horizontal lines.

For this case, the model predictions also line up with the experimental results to within a standard deviation. However, model predictions average slightly lower than the experimental measurements, particularly parallel to the scan direction. Despite some small oscillations that occur at the boundaries of each layer, the model predicts residual stresses that stay essentially constant throughout the height of the part and then fall off quickly near the free surface. Although the magnitude of the stresses measured by Yadroitsava are larger, especially parallel to the scan direction, this is the same general trend in the data as well, as the stresses measured near the substrate and 100 μm from the surface are almost overlapping. The spacing of the measurements is too coarse to be able to verify the layer oscillations that are seen in the model.

Two possible reasons for the difference between the stress predictions and measurements, particularly parallel to the scan direction are that the continuum model does not account for the motion of the metal and air that occurs when the powder melts. Thus the melted powder remains a mixture of metal and air, with correspondingly reduced values for stiffness, as opposed to the air escaping the melt as happens in reality. This reduced stiffness could account for the lower residual stresses, an effect that would be more apparent the more layers modeled. Additionally, the powder in the simulation is modeled as having an arbitrarily low stiffness, providing no resistance to the deformation of the melt at the interface between the two. In reality, the powder may in fact provide some significant resistance, reducing the amount the part is able to deform and thus increasing the residual stress.

Calculated uncertainties are relatively large for all cases, indicating the difficultly of making precise predictions about additive processes. The results of the VBD analysis allows the uncertainties due to each individual parameter to be ranked. Figs. 9 and 10 show the VBD of the stress parallel to the scan direction at the baseplate and at the free surface, respectively, for the 5 layer build. As can be seen, the uncertainty is dominated by the yield stress and effective absorptivity at the baseplate and by the yield stress alone at the free surface. As the sum of the main effects is very nearly one for both cases, these parameters contribute to the uncertainty almost completely on their own, not in interactions with other parameters.

That effective absorptivity contributes to a large uncertainty near the baseplate but not near the surface may be because the stress near the baseplate is strongly influenced by the stress field in the baseplate, which is governed by thermal stresses due to the amount of energy absorbed. The free surface, however, is far enough away from the plate

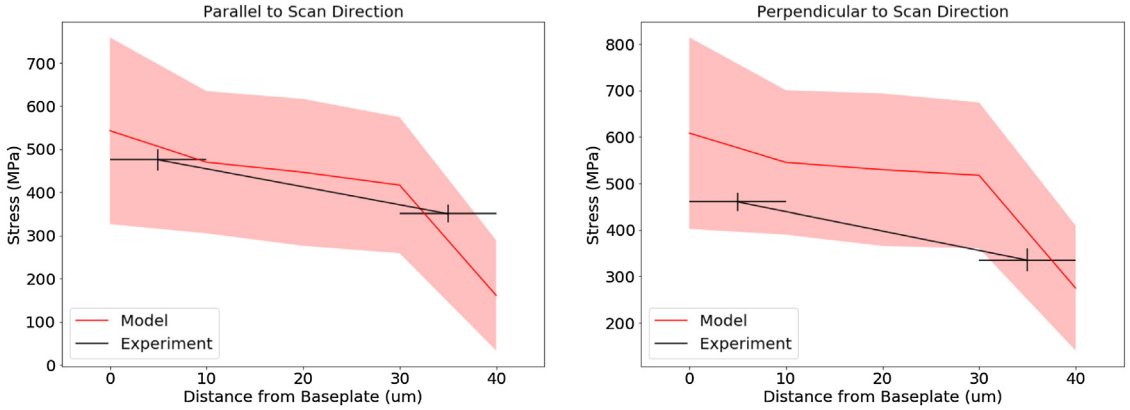

Fig. 7. Predicted residual stress profiles parallel to and perpendicular to laser scan direction for a single layer. Top of powder bed is at 40 μm from the top of the baseplate. Horizontal lines show the range of Yadroitsava's measurements near the plate and near the free surface.

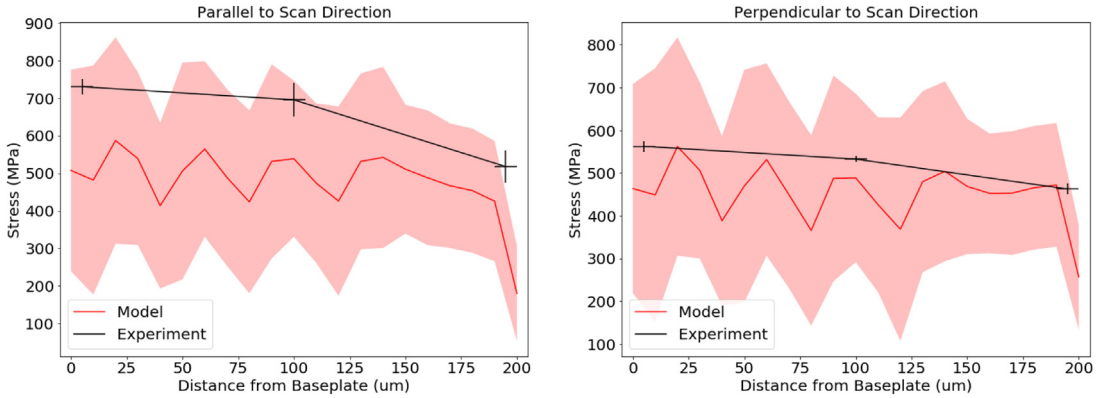

Fig. 8. Predicted residual stress profiles parallel to and perpendicular to laser scan direction for 5 layers. Top of powder bed is at 200 μm. Horizontal lines show the range of Yadroitsava's measurements near the plate, 100 μm from the surface, and near the free surface.

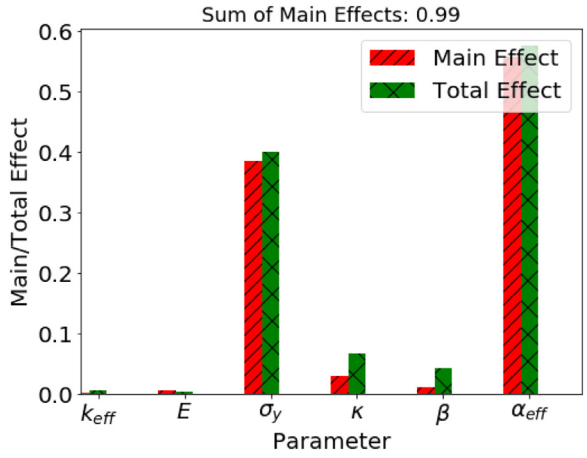

Fig. 9. Variance based decomposition of stress parallel to scan direction at the baseplate.

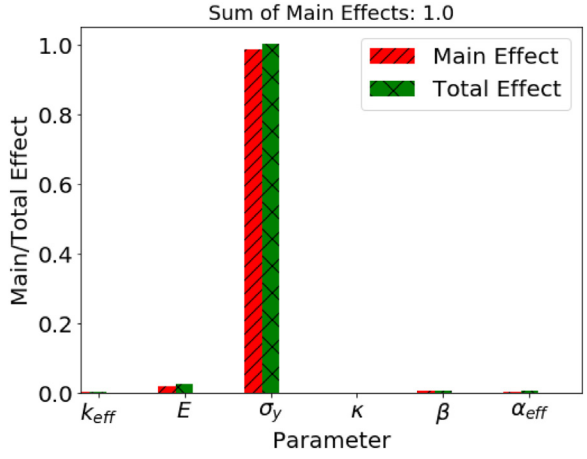

Fig. 10. Variance based decomposition of stress parallel to scan direction at the free surface.

for this effect not to be felt. VBD of the other stress predictions is also performed, but the results are very similar, so are not shown here.

Uncertainties in the model may be underestimated due to un-modeled physics in the framework, such as the complexities of the melt flow which lead to variable melt track shapes that are not captured or estimated here. Additionally, microstructure formation is not modeled, which can contribute to significant variability in material properties for additively manufactured components. The large contribution of yield stress to the uncertainty underscores the importance of modeling the microstructure in order to reduce the uncertainty on this parameter. Finally, residual stress data for additively manufactured materials is difficult to obtain, scarce in the literature, and also prone to large uncertainties. More data to compare against would allow a better assessment of the experimental uncertainty and whether the model's estimated uncertainties are correctly capturing the experimental variation. However, the multi-scale uncertainty quantification framework developed here provides a tool for estimating how process uncertainties at the particle-scale effect the knowledge of quantities of interest at the part-scale. Future work should incorporate additional particle-scale physics and microstructure formation so that better predictions and uncertainty estimates can be made.

4. Conclusion

A continuum thermo-mechanical model of the SLM process is presented. Particle-scale SLM models are used to calculate parameters of the developed continuum thermal model. This demonstrates a framework by which continuum level models can be informed with particle-scale physics, providing a mechanism for computationally expensive particle-scale models to be used to improve predictions at the continuum scale. Additionally, by using the Gaussian surrogate model technique to propagate uncertainties through the continuum model, the impact of particle-scale uncertainties can be calculated for the continuum prediction. This allows a quantitative comparison to experimental data. The developed continuum model is able to make residual stress predictions that agree with experimental measurements to within the estimated uncertainties for a single layer and for 5 layers. However, predicted means tend to be lower when compared to measured values for 5 layers, perhaps due to un-modeled physics in the melting process. Estimated uncertainties from the model are large, coming both from the uncertainty in the measurement location and the input parameter uncertainty, which is dominated by the yield stress and effective absorptivity parameters, making precise residual stress predictions difficult. The importance of yield stress uncertainty highlights the need for high-fidelity microstructure models to inform mechanical properties, similar to how thermal properties have been informed here. Experimental improvements may also be possible to reduce uncertainties on the data side, although many uncertainties arise from the powder-based nature of the process itself, where exact knowledge of powder particle locations, sizes, and shapes is impossible. This highlights the challenges of making credible predictions in SLM models and the need for further incorporation of uncertainty quantification into SLM modeling.

Declaration of Competing Interest

The authors declare that they have no known competing financial

interests or personal relationships that could have appeared to influence the work reported in this paper.

Acknowledgments

Sandia National Laboratories is a multimission laboratory managed and operated by National Technology & Engineering Solutions of Sandia, LLC, a wholly owned subsidiary of Honeywell International Inc., for the U.S. Department of Energy National Nuclear Security Administration under contract DE-NA0003525. The views expressed in the article do not necessarily represent the views of the U.S. Department of Energy or the United States Government.

References

[1] W.E. Frazier, Metal Additive manufacturing: a review, J. Mater. Eng. Perform. 23 (6) (2014) 1917–1928, https://doi.org/10.1007/s11665-014-0958-z.

[2] W.E. King, A.T. Anderson, R.M. Ferencz, N.E. Hodge, C. Kamath, S.A. Khairallah, A.M. Rubenchik, Laser powder bed fusion additive manufacturing of metals; physics, computational, and materials challenges, Appl. Phys. Rev. 2 (4) (2015) 41304, https://doi.org/10.1063/1.4937809.

[3] S. Sun, L. Zheng, Y. Liu, J. Liu, H. Zhang, Selective laser melting of Al-Fe-V-Si heat-resistant aluminum alloy powder: modeling and experiments, Int. J. Adv. Manuf. Technol. 80 (9) (2015) 1787–1797, https://doi.org/10.1007/s00170-015-7137-8.

[4] K. Zeng, D. Pal, H. Gong, N. Patil, B. Stucker, Comparison of 3DSIM thermal modelling of selective laser melting using new dynamic meshing method to ANSYS, Mater. Sci. Technol. 31 (8) (2015) 945–956.

[5] N.E. Hodge, R.M. Ferencz, J.M. Solberg, Implementation of a thermomechanical model for the simulation of selective laser melting, Comput. Mech. 54 (1) (2014) 33–51, https://doi.org/10.1007/s00466-014-1024-2.

[6] S.A. Khairallah, A.T. Anderson, A. Rubenchik, W.E. King, Laser powder-bed fusion additive manufacturing: physics of complex melt flow and formation mechanisms of pores, spatter, and denudation zones, Acta Mater. 108 (2016) 36–45, https://doi.org/10.1016/j.actamat.2016.02.014.

[7] D. Moser, S. Pannala, J. Murthy, Computation of effective radiative properties of powders for selective laser sintering simulations, JOM 67 (5) (2015) 1194–1202, https://doi.org/10.1007/s11837-015-1386-8.

[8] D. Moser, S. Pannala, J. Murthy, Computation of effective thermal conductivity of powders for selective laser sintering simulations, J. Heat Transf. 138 (8) (2016) 82002, https://doi.org/10.1115/1.4033351.

[9] D. Moser, A. Yuksel, M. Cullinan, J. Murthy, Use of detailed particle melt modeling to calculate effective melt properties for powders, J. Heat Transf. 140 (5) (2018), https://doi.org/10.1115/1.4038423 052301-052301-11.

[10] B.M. Adams, M.S. Ebeida, M.S. Eldred, G. Geraci, J.D. Jakeman, K.A. Maupin, J.A. Monschke, J.A. Stephens, L.P. Swiler, D.M. Vigil, T.M. Wildey, W.J. Bohnhoff, K.R. Dalbey, J.P. Eddy, J.R. Frye, R.W. Hooper, K.T. Hu, P.D. Hough, M. Khalil, E.M. Ridgway, J.G. Winokur, A. Rushdi, DAKOTA, a Multilevel Parallel Object-Oriented Framework for Design Optimization, Parameter Estimation, Uncertainty Quantification, and Sensitivity Analysis: Version 6.8 User's Manual, Sandia Technical Report SAND2014-4, (2018).

[11] C.R. Swaminathan, V.R. Voller, A general enthalpy method for modeling solidification processes, Metall. Trans. B 23 (5) (1992) 651–664, https://doi.org/10.1007/BF02649725.

[12] J.C. Nelson, S. Xue, J.W. Barlow, J.J. Beaman, H.L. Marcus, D.L. Bourell, Model of the selective laser sintering of bisphenol-A polycarbonate, Ind. Eng. Chem. Res. 32 (10) (1993) 2305–2317, https://doi.org/10.1021/ie00022a014.

[13] M. Negahban, The Mechanical and Thermodynamical Theory of Plasticity, first edition, CRC Press, Boca Raton, FL, 2012.

[14] OpenFOAM Foundation, OpenFOAM User Guide, (2016) http://foam.sourceforge.net/docs/Guides-a4/OpenFOAMUserGuide-A4.pdf.

[15] F. Moukalled, L. Mangani, M. Darwish, The Finite Volume Method in Computational Fluid Dynamics, Springer International Publishing, 2016, https://doi.org/10.1007/978-3-319-16874-6.

[16] I. Yadroitsava, I. Yadroitsev, Residual stress in metal specimens produced by direct metal laser sintering, Proceedings of Solid Freeform Fabrication Symposium (2015) 614–626.

[17] S.A. Khairallah, A. Anderson, Mesoscopic simulation model of selective laser melting of stainless steel powder, J. Mater. Process. Technol. 214 (11) (2014) 2627–2636, https://doi.org/10.1016/j.jmatprotec.2014.06.001.

[18] T.M. Mower, M.J. Long, Mechanical behavior of additive manufactured, powder-bed laser-fused materials, Mater. Sci. Eng. A 651 (2016) 198–213, https://doi.org/10.1016/J.MSEA.2015.10.068.

[19] D. Moser, S. Fish, J. Beaman, J.Y. Murthy, Multi-layer computational modeling of selective laser sintering processes, Proceedings of the ASME 2014 International Mechanical Engineering Congress & Exposition (2014).

[20] B.M. Adams, M.S. Ebeida, M.S. Eldred, G. Geraci, J.D. Jakeman, K.A. Maupin, J.A. Monschke, J.A. Stephens, L.P. Swiler, D.M. Vigil, T.M. Wildey, W.J. Bohnhoff, K.R. Dalbey, J.P. Eddy, J.R. Frye, R.W. Hooper, K.T. Hu, P.D. Hough, M. Khalil, E.M. Ridgway, J.G. Winokur, A. Rushdi, DAKOTA, a Multilevel Parallel Object-Oriented Framework for Design Optimization, Parameter Estimation, Uncertainty Quantification, and Sensitivity Analysis: Version 6.8 Theory Manual, Sandia Technical Report SAND2014-4, (2018).